# CMS Physics Analysis Summary

Contact: cms-pag-conveners-exotica@cern.ch 2016/08/05

# Search for resonant production of high mass photon pairs using 12.9 $\text{fb}^{-1}$ of proton-proton collisions at $\sqrt{s} = 13$ TeV and combined interpretation of searches at 8 and 13 TeV

The CMS Collaboration

## Abstract

We report on a search for resonant production of high mass photon pairs. The search employs 12.9 $\text{fb}^{-1}$ of pp collision data collected by the CMS experiment in 2016 at a centre-of-mass energy of 13 TeV. It is aimed at spin-0 and spin-2 resonances of mass between 0.5 and 4.5 TeV and width, relative to the mass, up to $5.6 \times 10^{-2}$. The results of the search are combined statistically with those previously obtained by the CMS collaboration at $\sqrt{s} = 8$ and 13 TeV. Limits are set on scalar resonances produced through gluon-gluon fusion, and on Randall–Sundrum gravitons. No significant excess is observed over the standard model predictions.

# 1 Introduction

The resonant production of high-mass photon pairs is a prediction that arises in several extensions of the standard model (SM) of particle physics. The spin of a resonance decaying to two photons must be either 0 or an integer greater than or equal to 2 [1, 2]. Spin-0 resonances decaying to two photons are predicted by models with nonminimal Higgs sectors [3, 4], while spin-2 resonances decaying to two photons can arise in models with additional space-like dimensions [5].

Theories that introduce additional space-like dimensions provide an approach to solve the so-called hierarchy problem, which has its origin in the large difference between the scale of the electroweak and of the gravitational interactions. The existence of additional dimensions has the effect of "diluting" gravity and thus allows lowering of the scale of the gravitational interaction and avoidance of the hierarchy problem.

The Randall-Sundrum (RS) approach to extra-dimensions postulates the presence of two brane-worlds [5]. The SM fields are allowed to propagate only in one of the two branes, whereas the gravitational field can propagate in both. The further assumption of a warped space-time metric allows the difference between the electroweak and Planck scales to be accounted for. From the phenomenological point of view, the excitations of the gravitational field leads to "towers" of spin-2 resonances, commonly denoted as gravitons, separated by a characteristic mass scale [6] that is large enough to allow the independent observation of each resonance.

The simplest extension of the SM Higgs sector consists in the addition of a second doublet of scalar fields to the theory. Models of this kind, known as two-Higgs-doublet models (2HDM) [7] feature the presence of a total of five scalar or pseudo-scalar resonances in the spectrum of the theory. Identifying one of the scalars as the 125 GeV Higgs boson discovered by the CMS and ATLAS collaborations [8, 9], and assuming that its couplings correspond to those of the SM Higgs boson, forces the 2HDM in the so-called alignment limit [10] where some of the additional resonances can decay to a photon pair at a non-negligible rate.

Recently, the ATLAS [11] and CMS [12] collaborations published the first results on searches for diphoton resonances at $\sqrt{s}$ = 13 TeV, based on data collected in 2015, which correspond to an integrated luminosity of about 3 $\text{fb}^{-1}$ for each experiment. Both analyses reported the observation of a modest deviation from the background-only expectation, compatible with the production of a resonance with a mass of around 750 GeV.

Searches for RS graviton production were performed at $\sqrt{s} = 7$, 8, and 13 TeV by the CMS and ATLAS collaborations in a variety of final states [13–29]. Searches for spin-0 particles decaying to two photons were also performed by the CMS and ATLAS collaborations at lower centre of mass energies [19, 30].

In this note we report on the search for spin-0 resonances and RS gravitons in the diphoton final state using 12.9 $\text{fb}^{-1}$ of pp collisions collected by the CMS experiment in 2016 at $\sqrt{s}$ = 13 TeV. The analysis techniques employed in the search follow what was done in Ref. [12] for the 13 TeV data collected in 2015 and the results of the search are combined statistically with those in Ref. [12].

# 2 The CMS detector

The central feature of the CMS apparatus is a superconducting solenoid of 6 m internal diameter, providing a magnetic field of 3.8 T. Within the superconducting solenoid volume are a

silicon pixel and strip tracker, a lead tungstate crystal electromagnetic calorimeter (ECAL), and a brass and scintillator hadron calorimeter (HCAL), each composed of a barrel and two endcap sections. Forward calorimeters extend the pseudorapidity coverage provided by the barrel and endcap detectors. Muons are measured in gas-ionisation detectors embedded in the steel flux-return yoke outside the solenoid.

In the barrel section of the ECAL, an energy resolution of about 1% is achieved for unconverted or late-converting photons in the tens of GeV energy range. The remaining barrel photons have an energy resolution of about 1.3% up to a pseudorapidity of $|\eta| = 1$, rising to about 2.5% at $|\eta| = 1.4$. In the endcaps, the resolution of unconverted or late-converting photons is about 2.5%, while the remaining endcap photons have a resolution between 3 and 4% [31].

The particle-flow event algorithm [32, 33] reconstructs and identifies each individual particle with an optimised combination of information from the various elements of the CMS detector. The energy of photons is directly obtained from the ECAL measurement, correcting for radiative losses and containment effects. The energy of electrons is determined from a combination of the electron momentum at the primary interaction vertex as determined by the tracker, the energy of the corresponding ECAL cluster, and the energy sum of all bremsstrahlung photons spatially compatible with originating from the electron track. The energy of muons is obtained from the curvature of the corresponding track. The energy of charged hadrons is determined from a combination of their momentum measured in the tracker and the matching ECAL and HCAL energy deposits, corrected for zero-suppression effects and for the response function of the calorimeters to hadronic showers. Finally, the energy of neutral hadrons is obtained from the corresponding corrected ECAL and HCAL energy.

The first level of the CMS trigger system, composed of custom hardware processors, uses information from the calorimeters and muon detectors to select the most interesting events in a fixed time interval of less than 4 $\mu$s. The high level trigger processor farm further decreases the event rate from around 100 kHz to less than 1 kHz, before data storage.

A more detailed description of the CMS detector, together with a definition of the coordinate system used and the relevant kinematic variables, can be found in Ref. [34].

## 3 Data and simulated samples

The data considered in this analysis correspond to an integrated luminosity of 12.9 fb$^{-1}$ collected by the CMS experiment in 2016. The dataset fulfils standard quality criteria for all components of the CMS detector.

Simulated signal samples of spin-0 and spin-2 resonances decaying to two photons are generated at leading order (LO) with the PYTHIA 8.2 [35] event generator, using the NNPDF2.3 [36] parton distribution functions (PDFs), with values of the resonance mass $m_X$ in the range $0.5 < m_X < 4.5$ TeV. Three values of the relative width $\Gamma_X/m_X$ where chosen as benchmark: $1.4 \times 10^{-4}$, $1.4 \times 10^{-2}$ and $5.6 \times 10^{-2}$, corresponding respectively, to resonances much narrower than, comparable to, and significantly wider than the detector resolution. For the RS graviton model, where $\Gamma_X/m_X = 1.4\tilde{k}^2$ [6], this corresponds to dimensionless coupling values $\tilde{k} = 0.01, 0.1$, and 0.2. The principal SM background processes, namely the direct production of two photons ($\gamma\gamma$), the production of $\gamma$+jets events in which jet fragments are misidentified as photons, and the production of multijet events with misidentified jet fragments, are simulated with the SHERPA 2.1 [37], MADGRAPH5_AMC@NLO 2.2 [38] (interfaced with PYTHIA 8.2 for parton showering and hadronization), and PYTHIA 8.2 generators, respectively.

A detailed simulation of the CMS detector response to the events in the signal and background samples is performed using the GEANT4 package [39]. The average number of interactions per bunch crossing in the analysed dataset is 18, with an RMS of 4. Simulated events include the effect of multiple proton-proton interactions (pileup) taking place each bunch crossing and is weighted to reproduce the distribution of the number of interactions per bunch crossing in data.

## 4 Event selection and reconstruction

The event selection and photon identification criteria match those used in Ref. [12]. Events with at least two reconstructed photon candidates are selected and a search is made for a localised excess of events in the diphoton mass spectrum consistent with the resonant production of photon pairs.

The trigger selection requires at least two photon candidates of transverse momentum above 60 GeV. For these events, the ratio between the energy deposited in the hadron calorimeter towers behind each photon cluster and the photon energy ("H/E ratio") is required to be consistent with that expected from prompt photon candidates. The trigger selection is fully efficient for resonance masses above 500 GeV.

Photon candidates are reconstructed from energy deposits in the ECAL. Energy deposits compatible with the expected shower shape of electrons and photons are clustered together. The clustering algorithm does not make any hypothesis as to whether the particle originating from the interaction point is a photon or an electron. Thus the same algorithm used for photon reconstruction can be applied to $Z \to e^+e^-$ events and these events can be used to measure the efficiency of the photon selection criteria and of the photon energy scale and resolution.

In order to obtain the best energy resolution, the ECAL signals are calibrated and corrected for several detector effects. The variation of the crystal transparency during the run is corrected with a dedicated monitoring system and the single-channel response equalised using collision events [31]. The containment of the shower in the clustered crystals, the shower losses for photons that convert in the material upstream of the calorimeter, and the effects of pileup, are corrected for using a multivariate regression technique [31].

In the longitudinal direction, $z$, the interaction vertices, built from the reconstructed tracks, have a distribution with an RMS spread of about 3.5 cm. The diphoton mass resolution has contributions from the resolution of the measurement of the photon energies and the measurement of the angle between the two photons.If the vertex from which the photons originate is known to within about 10 mm, then the experimental resolution on the angle between them gives a negligible contribution to the mass resolution. Associating the diphoton with one of the vertices reconstructed from the charged particle tracks in the event satisfies this requirement since the position of these vertices is measured with far greater precision.The interaction vertex is selected using the algorithm described in Refs. [40], which combines informations on the correlation between the diphoton system and the recoiling tracks, the average transverse momentum of the recoiling tracks, and, when available, the pointing informations from reconstructed $e^+e^-$ conversions. For resonances of masses above 500 GeV, the fraction of events in which the interaction vertex is correctly assigned is approximately 90%.

In each event, photon candidates with $p_T > 75$ GeV are grouped in all possible pairs, which are required to satisfy the following kinematic criteria:

- The $p_T$ of both candidates is required to be above 75 GeV.

- The absolute value of the pseudorapidity of both candidates, computed with respect to centre of the CMS detector and denoted $|\eta_C|$ in the following, is required to be below 2.5 and not between 1.44 and 1.57.
- At least one of the photon candidates is required to have $|\eta_C|$ below 1.44 (i.e. events with both photon candidates in the ECAL endcaps region are rejected).
- The invariant mass of the pair, $m_{\gamma\gamma}$, is required to be above 230 GeV. For events where one photon candidate is in an endcap, $m_{\gamma\gamma} > 330$ GeV is required.

Each of the photon candidates in all pairs is further required to satisfy a set of identification criteria:

- The transverse size of the electromagnetic cluster in the $\eta$ direction is required to be compatible with that expected from prompt photons.
- The H/E ratio is required to be less than 0.05.
- The sum of the transverse momenta of particle-flow charged hadron candidates, assigned to the chosen primary vertex, and contained in a cone of radius 0.3 in $\eta, \phi$ space centred on the photon candidate is required to be below 5 GeV. Charged particle-flow candidates compatible with conversion tracks associated with the photon candidate are excluded from the sum.
- The sum of the transverse energy of additional photon candidates contained in regions of radius 0.3 in $\eta, \phi$, corrected for pileup effects, is required to be below 2.5 GeV.
- The candidate is rejected in case it is associated with an electron track incompatible with an $e^+e^-$ conversion.

The efficiency of the identification criteria for prompt isolated photon candidates, in the kinematic range considered by the analysis, is above 90(85)% in the barrel (endcaps). The identification and trigger efficiencies are measured, as a function of $p_T$, using data events containing a Z boson decaying to a pair of electrons, or to a pair of electrons or muons in association with a photon [31]. The efficiencies measured in data are found to be 3.5% and 6.5% lower than predicted for photons in the barrel and endcap regions respectively. A correction factor is applied to simulated events to take this into account.

The fraction of events where more than one photon pair satisfies the selection criteria is roughly 1%. In these cases, only the pair with the largest scalar sum of photon momenta is retained. Photon pairs are split into two categories: the first, denoted "EBEB" in the following, contains pairs where both candidates are reconstructed in the ECAL barrel, while the second, denoted "EBEE", contains pairs where one of the candidates is reconstructed in an ECAL endcap. The overall fraction of signal events selected by the analysis varies between 0.5 and 0.7 depending on the signal hypothesis. Because of the different angular distribution of the decay products, the kinematic acceptance for the RS graviton resonances is lower than for scalar resonances; for $m_X < 1$ TeV the reduction is approximately 20%. The two acceptances become similar for $m_X > 3$ TeV.

The event selection criteria were determined using simulated signal and background samples and fixed prior to inspecting the diphoton invariant mass distribution in the search region, which is defined as $m_{\gamma\gamma} > 500$ GeV. The level of agreement between data and simulation was assessed before inspecting the diphoton invariant mass distribution in the search region. The evaluation was performed by checking other distributions in the search region, as well as all distributions for events outside of the search region. The event selection efficiencies were

measured in data and compared with expectations and the ratio of the total number of expected and observed events in the search region were checked as part of the procedure. None of these assessments led to a change in the selection criteria that were determined using simulated events.

# 5 Determination of the photon energy scale and resolution

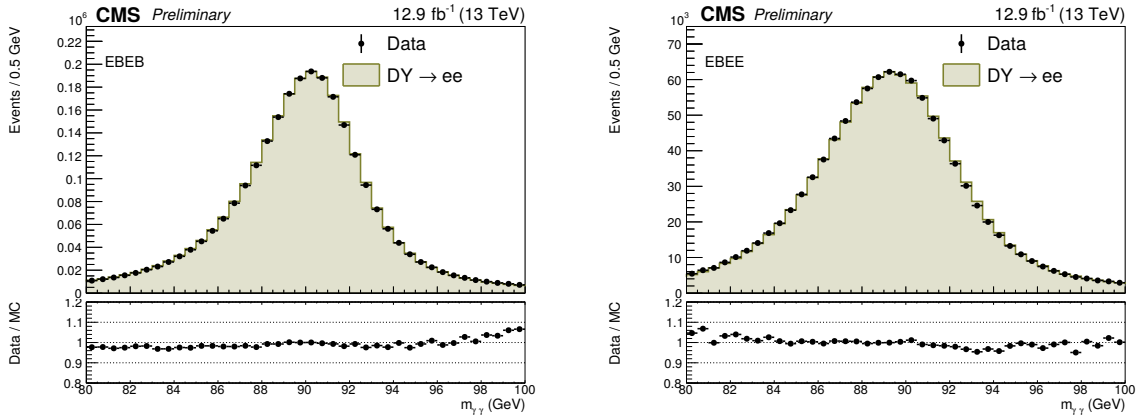


Figure 1: Comparison between the predicted and observed invariant mass distribution of electron pairs obtained after the application of energy scale, resolution and identification efficiency corrections. Distributions are shown for events where both electrons are reconstructed in the barrel (left) and events where one electron is in an endcap (right).

As described above, the energy of the photon candidates is assigned using a multivariate regression. The corrections are tuned on photon candidates mostly of lower energies than those entering the analysis. For this reason the energy scale of photons above $\approx 200\,\text{GeV}$ deviates slightly from unity. The residual shift, due to the energy dependence of the longitudinal non-containment of the photon shower, is below 0.5% up to energies of $\approx 500\,\text{GeV}$ and below 1% up to energies of $\approx 1.5\,\text{TeV}$.

Discrepancies in the photon energy scale and resolution between data and simulation are resolved using $Z \to e^+e^-$ events, through the procedure described in Ref. [31]. The corrections are derived in eight bins defined in terms of the $R_9$ variable (defined as the ratio between the energy deposited in the central 3x3 crystal matrix and the full cluster energy) and of $|\eta_C|$.

The size of the energy scale corrections derived from $Z \to e^+e^-$ events varies between 0.2% and 1.2% in the region where $|\eta_C| < 2$ and it can be as high as 2% for $2 < |\eta_C| < 2.5$. The additional Gaussian smearing needed to match the energy resolution in simulated events with that in data varies between roughly 0.8% and 1.5% for photon candidates in the ECAL barrel region and between 2% and 2.5% for photon candidates in the endcap regions.

The dielectron invariant mass distribution obtained, for data and simulated events, after the adjustment procedure is shown in Fig. 1. To obtain these distributions, events containing pairs of photon candidates which satisfy the identification criteria used in the analysis and which are associated with electron tracks are selected. The identification efficiency corrections described in Sec. 4 are applied to simulated events for the comparison. A good agreement between data and simulation is observed both in terms of shape and normalisation.

The variation of the correction factors as a function of the energy of the photon candidate is assessed using $Z \to e^+e^-$ events in which the Z boson is produced at high transverse mo-

mentum. This allows to test the transverse energy range up to roughly 150(100) GeV in the barrel (endcap) region. For the barrel region, the energy scale corrections are found to be stable within 0.4% in the probed range. A stability better than 0.8% is observed for photon candidates in the endcaps.

# 6 Selected data sample and interpretation of the results

A total of 6284 (2791) photon pairs are selected in the EBEB (EBEE) category. Out of these, 461 (800) pairs have an invariant mass above 500 GeV. The invariant mass distribution of the selected events is shown in Fig. 2. A parametrisation of the spectrum of the form $f(m_{\gamma\gamma}) = m_{\gamma\gamma}^{a+b\cdot\log(m_{\gamma\gamma})}$, obtained through an unbinned maximum likelihood fit to the selected events, is shown. This parametric form corresponds to the one chosen to model the background in the hypothesis tests, as detailed in Section 8.

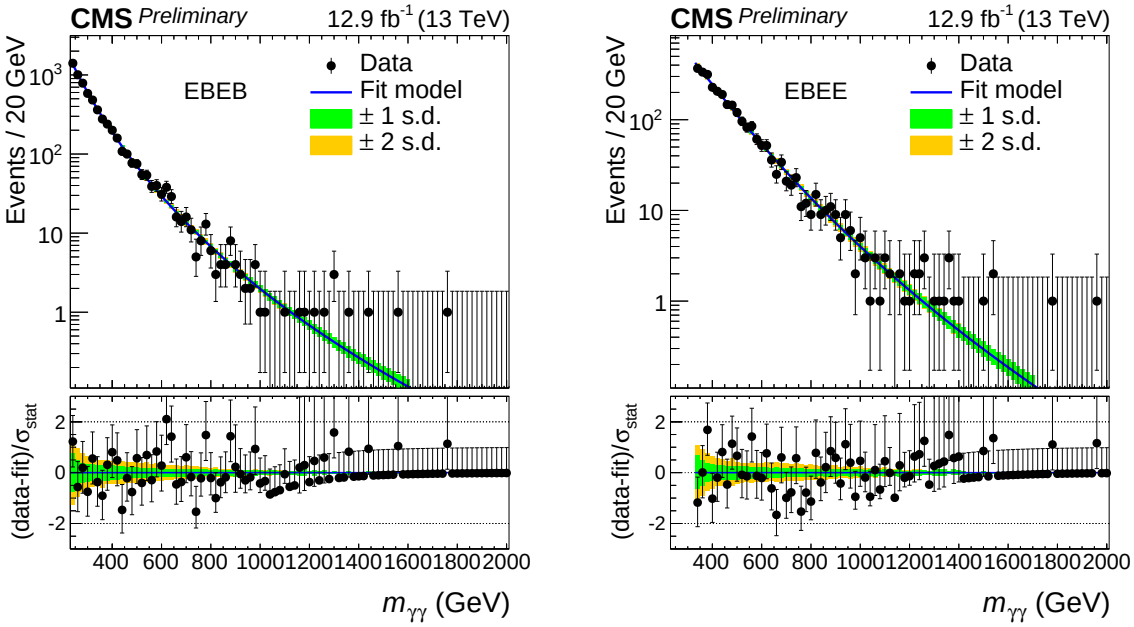


Figure 2: Observed invariant mass spectra for the EBEB (left) and EBEE (right). No event with $m_{\gamma\gamma} > 2000$ GeV is selected in the analysis. The results of a likelihood fit to the background-only hypothesis are also shown. The shaded regions show the 1 and 2 standard deviation uncertainty bands associated with the fit, and reflect the statistical uncertainty of the data. The lower panels show the difference between the data and fit, divided by the statistical uncertainty in the data points.

The results of the search are interpreted in the framework of a composite statistical hypothesis test. A simultaneous fit to the invariant mass spectra of the EBEB and EBEE event categories is used to study the compatibility of the data with the background-only and the signal+background hypotheses.

The test statistics used in the hypothesis tests are based on the profile likelihood ratio:

$$q(\mu) = -2log\frac{L(\mu \cdot S + B|\hat{\underline{\theta}}_{\mu})}{L(\hat{\mu} \cdot S + B|\hat{\underline{\theta}})}$$

where $S$ and $B$ are the probability density functions for the resonant diphoton production pro-

cess and the SM backgrounds respectively, $\mu$ is the so-called "signal strength" parameter and $\underline{\theta}$ are the nuisance parameters of the model, used to account for the associated systematic uncertainties. The $\hat{x}$ notation indicates the best-fit value of the parameter x, while the notation $\hat{x}_y$ denotes the best-fit value of x, conditionally on y.

To set upper limits on the resonant diphoton production rate, the modified frequentist method, commonly known as $CL_s$ [41, 42], is used following the prescription described in Ref. [43].

The compatibility of the observation with the background-only hypothesis is evaluated computing the background-only $p$-value. The latter is defined as the probability, in the background-only hypothesis, for $q(0)$ to be above the observation. This quantity, the "local $p$-value" $p_0$, does not take into account the fact that many signal hypotheses are tested.

Asymptotic formulas [44] are used in the calculations of limits and local $p$-values. The accuracy of the formulas in the estimation of limits and significance is studied for a subset of the hypothesis tests and is found to be about 10%.

# 7 Signal modelling

The signal distribution in $m_{\gamma\gamma}$ is determined from the convolution of the intrinsic shape of the resonance and the ECAL detector response. The intrinsic shape of the resonant signals are derived using the PYTHIA generator. A fine grid of mass points with 125 GeV spacing is used and the resulting shapes interpolated to intermediate points using a parametric description of the distribution. The detector response is determined using fully simulated signal samples of small intrinsic width and corrected for the additional Gaussian smearing determined from dielectron events. Nine equidistant mass hypotheses in the range 500-4500 GeV are employed. The signal mass resolution, quantified through the ratio of the full width at half maximum (FWHM) of the distribution, divided by 2.35, to the peak position, is roughly 1% and 1.5% for the EBEB and EBEE categories respectively.

In order to determine the signal normalisation, the efficiency of the final event selection is combined with the kinematic acceptance. The first is obtained from fully simulated samples and interpolated using a quadratic function of the resonance mass, after applying the efficiency correction factors measured in Z events. The second is obtained from the finely spaced grid of samples and parametrised as a quadratic function of both the resonance mass and width.

# 8 Background modelling

The background $m_{\gamma\gamma}$ spectrum is described by a parametric function of $m_{\gamma\gamma}$. The parametric coefficients are obtained from a fit to the data events, and considered as unconstrained nuisance parameters in the hypothesis test, allowing the building a data-driven description of the shape.

The accuracy of the background determination is assessed using MC simulations and it is quantified by studying the difference between the true and predicted number of background events in several $m_{\gamma\gamma}$ interval in the search region. The relative width of such regions ranges between 2% and 15%. Pseudo-experiments are drawn from the mass spectrum predicted by MC simulation. The total number of events in each pseudo-experiment is taken from a Poisson distribution where the mean is determined by the observation in data. For each interval, the distribution of the pull variable, defined as the difference between the true and predicted number of events divided by the estimated statistical uncertainty, is constructed. If the absolute value of the median of this distribution is found to be above 0.5 in a window, an additional

uncertainty is assigned to the background parametrisation. A modified pull distribution is then constructed increasing the statistical uncertainty on the fit by an extra term, denoted "bias term", which is parametrised as a smooth function of $m_{\gamma\gamma}$, tuned in such a way that the absolute value of the median of the modified pull distribution is below 0.5 for all regions. The additional uncertainty is then included in the likelihood function by adding to the background model a component having the same shape as the signal, with a normalisation coefficient distributed as a Gaussian of mean zero and width equal to the integral of the bias term over the FWHM of the tested signal shape. The inclusion of the additional component has the effect of avoiding falsely positive or negative tests that could be induced by a mismodeling of the background shape, and it degrades the analysis sensitivity by 10% or less.

## 9 Systematic uncertainties

The impact of the systematic uncertainties on this analysis is smaller than that of the statistical uncertainties. The parametric background model has no associated systematic uncertainties, except for the bias term uncertainty described above. The shape coefficients are treated as unconstrained nuisance parameters, thus the associated uncertainties contribute to the statistical uncertainty.

Uncertainties associated to the signal modelling are summarised here:

- Integrated luminosity. A 6.2% uncertainty on the signal normalisation is assigned to reflect the uncertainty on the knowledge of the total integrated luminosity.
- Selection efficiency uncertainties. A 6% uncertainty on the signal normalisation is included to reflect the uncertainty on the knowledge of the selection efficiency.
- Parton distribution functions. A 6% uncertainty on the signal normalisation is assigned in order to account for the variation in the kinematic acceptance of the analysis coming from the use of alternative PDF sets.
- Photon energy scale uncertainty. A 1% uncertainty on the knowledge of the energy scale uncertainty is included in fit. This number takes into account the knowledge of the energy scale at the Z peak and of its extrapolation to higher masses.
- Photon energy resolution uncertainty. The uncertainty on the resolution correction factors is evaluated summing and subtracting 0.5% in quadrature from the estimated additional Gaussian smearing measured at the Z peak.

## 10 Search results with an integrated luminosity of 12.9 fb$^{-1}$

Expected and observed upper limits on the production of scalar and RS graviton resonances are shown in Fig. 3. Using the LO cross sections from PYTHIA 8.2, RS gravitons with masses below 1.75, 3.75, and 4.35 TeV are excluded for $\tilde{k} = 0.01$, 0.1, and 0.2, respectively, corresponding to $\Gamma_X/m_X = 1.4 \times 10^{-4}$, $1.4 \times 10^{-2}$, and $5.6 \times 10^{-2}$.

The value of $p_0$ for different signal hypotheses is shown in Fig. 4. The largest excess is observed for $m_X$ of about 620 GeV, and has a local significance of roughly 2.4 and 2.7 standard deviations for narrow spin-0 and RS graviton signal hypotheses respectively. After taking into account the effect of searching for several signal hypotheses, the significance of the excess is reduced to less than one standard deviation. No excess is observed in the proximity of $m_X = 750$ GeV.

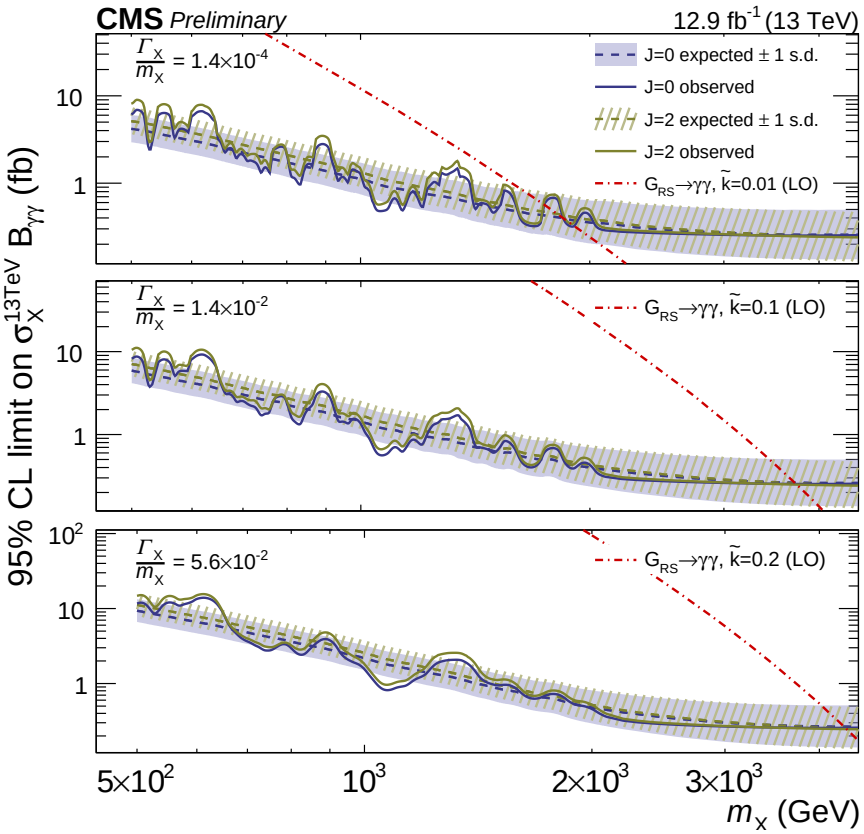


Figure 3: The 95% CL upper limits on the production of diphoton resonances as a function of the resonance mass $m_X$, from the analysis of the 12.9 fb$^{-1}$ data collected in 2016 at 13 TeV. The blue-grey (darker) curves and the green (lighter) ones correspond to the scalar and RS graviton signals, respectively. Solid (dashed) curves represent the observed (median expected) exclusion limit. The expected results are shown with their 1 standard deviation dispersion bands. The leading-order RS graviton production cross section is shown by the red dot-dashed curves. The results are shown for (upper) a narrow, (middle) an intermediate-width, and (lower) a broad resonance, with the value of the width $\Gamma_X/m_X$, relative to the mass, indicated in the legend of each plot.

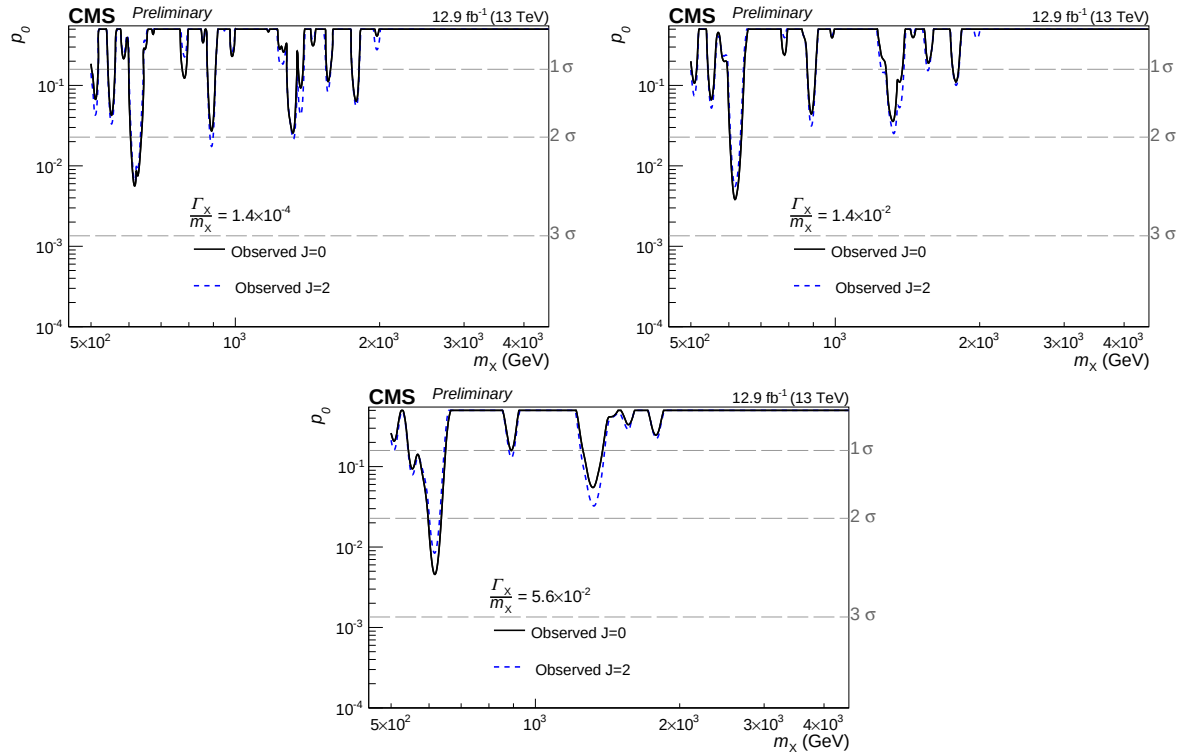


Figure 4: Observed background-only $p$-values for resonances with $\Gamma_X/m_X = 1.4 \times 10^{-4}$ (upper left), $1.4 \times 10^{-2}$ (upper right), and $5.6 \times 10^{-2}$ (lower) as a function of the resonance mass $m_X$, from the analysis of the 12.9 fb$^{-1}$ data collected at $\sqrt{s}$ =13 TeV in 2016. Solid black and dashed blue lines correspond to spin-0 and spin-2 resonances respectively.

# 11 Combination with previous results

The results obtained on the dataset analysed here, are combined statistically with those reported in Ref. [12], which analysed a total of 19.7 $\text{fb}^{-1}$ of proton-proton recorded at $\sqrt{s} = 8$ TeV in 2012 and 3.3 $\text{fb}^{-1}$ recorded at $\sqrt{s} = 13$ TeV in 2015, out of which 2.7 $\text{fb}^{-1}$ where taken while the CMS magnet was on (3.8 T), and the rest while it was off.

The combination procedure follows the same prescription used in Ref. [12]. The ratio of the 8 TeV to the 13 TeV production rate is computed, using PYTHIA 8.2 for the two types of signal hypotheses considered: scalar resonances produced through gluon-gluon fusion and RS graviton resonances produced through both gluon fusion and quark-antiquark annihilation. In the RS model, the first mechanism accounts for roughly 90% of the production cross section. The cross-section ratio decreases from 0.27 and 0.29 at $m_X = 500$ GeV to 0.03 and 0.04 at $m_X = 4$ TeV, for the scalar and RS graviton resonance, respectively.

Exclusion limits are set on the 13 TeV production cross section for both models and background-only $p$-values are computed for the same signal hypotheses described in Section 10.

The correlation model between the uncertainties associated with 8 TeV and 13 TeV data is described in details in Ref. [12], and it assumes all uncertainties to be uncorrelated, except for those related to the knowledge of the photon energy scale, taken to have a linear correlation of 0.5, and those related to the knowledge of the PDFs, taken to be fully correlated.

The background shape, and the associated bias term uncertainties, are assumed to be fully correlated between corresponding categories in the 13 TeV 3.8 T data from Ref. [12] and in the 12.9 $\text{fb}^{-1}$ data analysed here. Independent background normalisation coefficients are used for the two datasets.

The uncertainty on the signal selection efficiency is taken to be uncorrelated between the 2015 data and the 2016 data. The uncertainty on the knowledge of the integrated luminosity is treated as follows: a 2.7% uncertainty is taken to be fully correlated between 3.8 T 2015 data and 2016 data, and an additional 5.6% uncertainty is applied to 2016 data. Finally, the photon energy scale uncertainties are taken to be fully correlated between the two datasets.

Figure 5 shows the expected and observed 95% CL limits on the 13 TeV production cross-section of the different signal hypotheses obtained with the combined analysis of the 13 TeV data recorded in 2015 and 2016. Compared to the 2016 dataset alone, the combined analysis sensitivity improves by roughly 10 and 20% at the high and low end of the $m_X$ search region. Using the LO cross sections from PYTHIA 8.2, RS gravitons with masses below 3.85 and 4.45 TeV are excluded for $\tilde{k} = 0.1$ and 0.2, respectively. For $\tilde{k} = 0.01$, graviton masses below 1.95 TeV are excluded, except for the region between 1.75 TeV and 1.85 TeV.

The observed $p_0$ for $\Gamma_X/m_X = 1.4 \times 10^{-4}$ and $5.6 \times 10^{-2}$ obtained with the combined analysis of 2015 and 2016 data is shown in Fig. 6. The largest excess is observed for $m_X \approx 1.3$ TeV and it has a local significance of about 2.2 standard deviations, reduced to less than 1 standard deviation after accounting for the effect of searching for several signal hypotheses. For $m_X = 750$ GeV, the roughly 2.9 standard deviations excess observed in the 2015 data is reduced to about 0.8 standard deviations in the combined analysis.

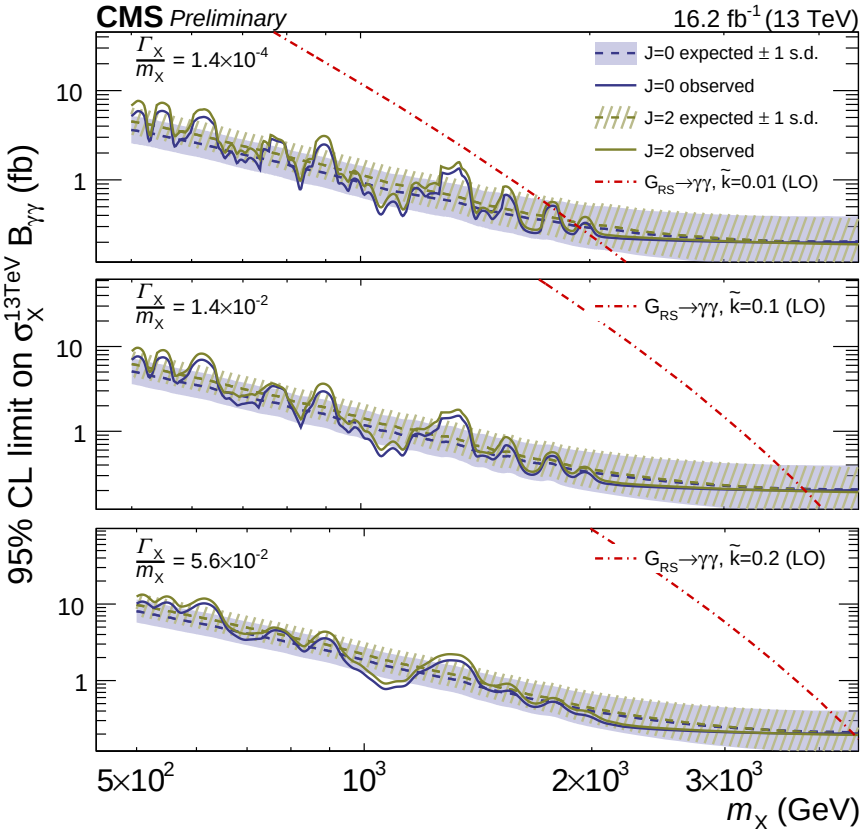


Figure 5: The 95% CL upper limits on the production of diphoton resonances as a function of the resonance mass $m_X$, from the combined analysis of the 13 TeV data collected in 2015 and in 2016. The blue-grey (darker) curves and the green (lighter) ones correspond to the scalar and RS graviton signals, respectively. Solid (dashed) curves represent the observed (median expected) exclusion limit. The expected results are shown with their 1 standard deviation dispersion bands. The leading-order RS graviton production cross section is shown by the red dot-dashed curves. The results are shown for (upper) a narrow, (middle) an intermediate-width, and (lower) a broad resonance, with the value of the width $\Gamma_X/m_X$, relative to the mass, indicated in the legend of each plot.

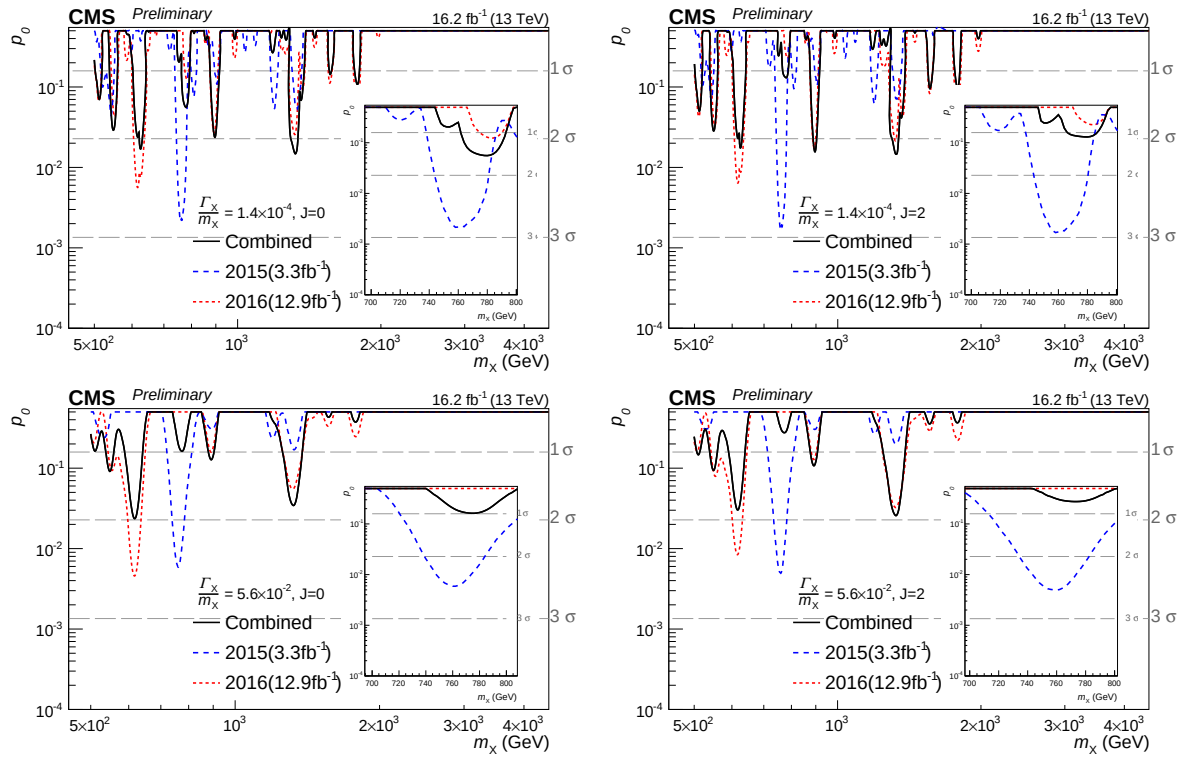


Figure 6: Observed background-only $p$-values for resonances with $\Gamma_X/m_X = 1.4 \times 10^{-4}$ (upper) and $5.6 \times 10^{-2}$ (lower) as a function of the resonance mass $m_X$, from the combined analysis of the 13 TeV data recorded in 2015 and 2016. The results obtained with the two individual datasets are also shown. Curves corresponding to the scalar and RS graviton hypotheses are shown in left and right columns respectively.

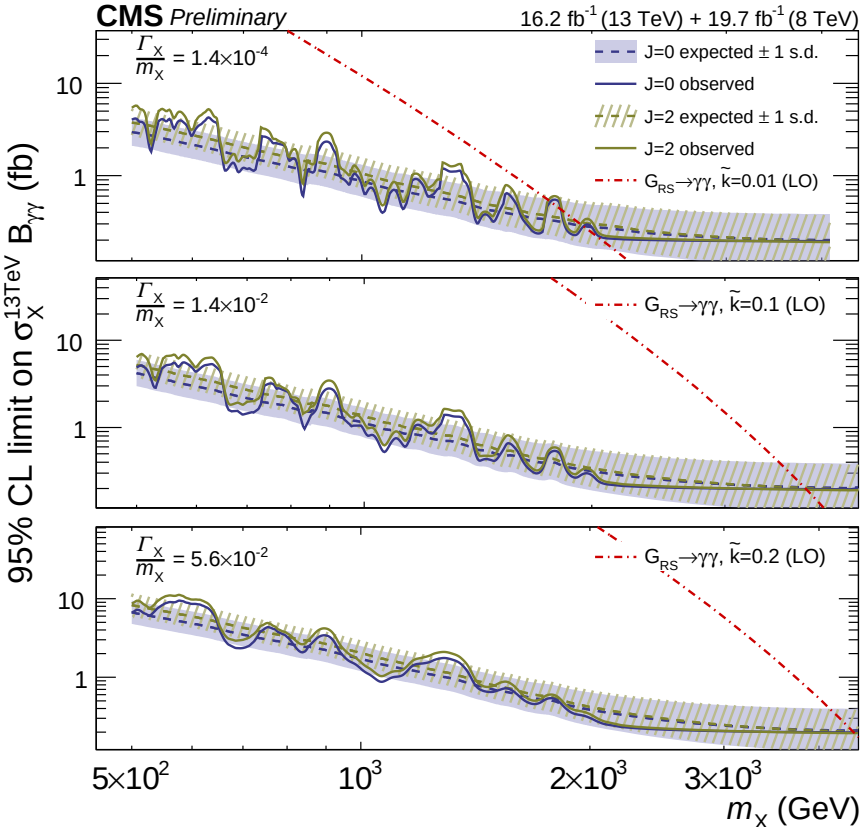


Figure 7: The 95% CL upper limits on the production of diphoton resonances as a function of the resonance mass $m_X$, from the combined analysis of the 8 and 13 TeV data. The 8 TeV results are scaled by the ratio of the 8 to 13 TeV cross sections. The blue-grey (darker) curves and the green (lighter) ones correspond to the scalar and RS graviton signals, respectively. Solid (dashed) curves represent the observed (median expected) exclusion limit. The expected results are shown with their 1 standard deviation dispersion bands. The leading-order RS graviton production cross section is shown by the red dot-dashed curves. The results are shown for (upper) a narrow, (middle) an intermediate-width, and (lower) a broad resonance, with the value of the width $\Gamma_X/m_X$, relative to the mass, indicated in the legend of each plot.

The expected and observed 95% CL limits on the 13 TeV signal production cross-sections obtained combining the results obtained on the 8 TeV and 13 TeV data are shown in Fig. 7. Compared to the sensitivity of the 13 TeV data, the analysis sensitivity improves by about 10% at the low end of the $m_X$ range, while the improvement is negligible at the higher end of the range. As consequence the lower exclusion limits on the mass of RS graviton resonances obtained combining 8 and 13 TeV data coincide with those obtained with 13 TeV data alone.

The observed $p_0$ for $\Gamma_X/m_X = 1.4 \times 10^{-4}$ and $5.6 \times 10^{-2}$ obtained with the combined analysis of 8 and 13 TeV data is shown in Fig. 8. The largest excess is observed for $m_X \approx 0.9$ TeV and it has a local significance of about 2.2 standard deviations, corresponding to less than 1 standard deviation overall. For $m_X = 750$ GeV, the 3.4 standard deviation excess reported in Ref. [12] is reduced to about 1.9 standard deviations.

The compatibility of the data with a common signal strength at $m_X = 750$ GeV is evaluated by performing a goodness of fit (g.o.f.) test comparing the best fit signal strengths to the narrow spin-0 signal hypothesis obtained in the three analysed data sets: 13 TeV data recorded in

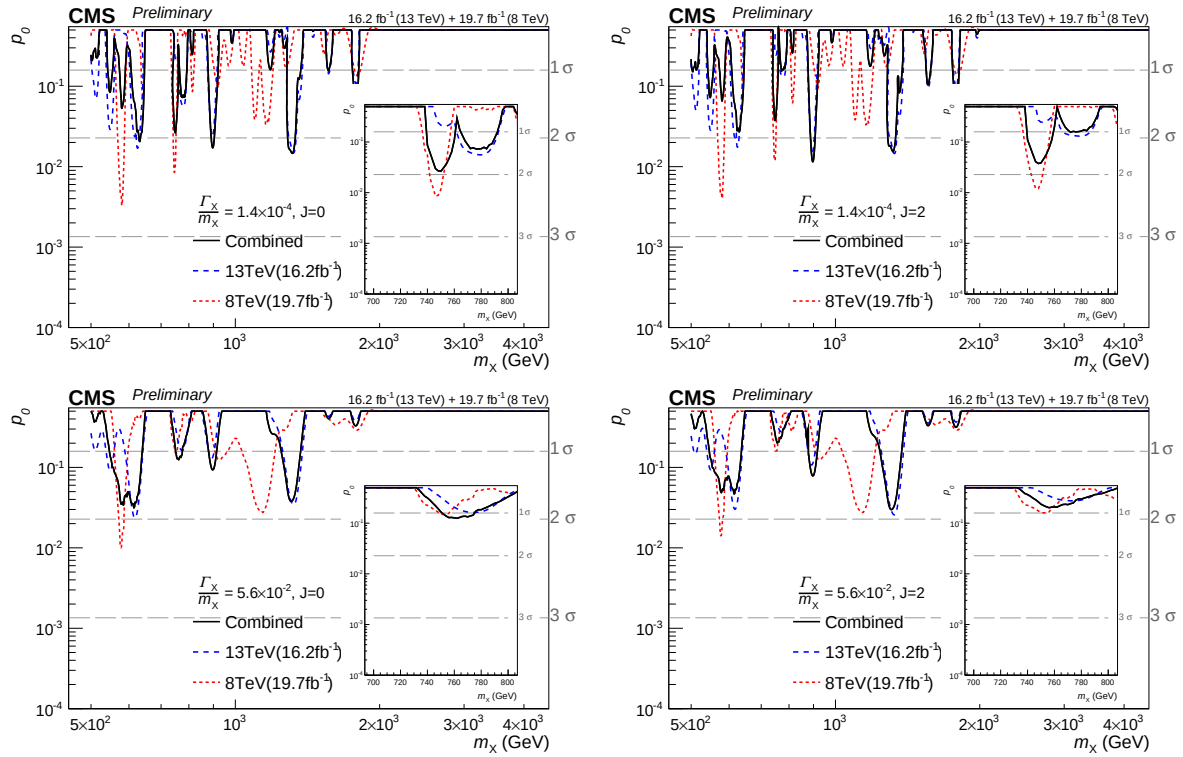


Figure 8: Observed background-only $p$-values for resonances with $\Gamma_X/m_X = 1.4 \times 10^{-4}$ (upper) and $5.6 \times 10^{-2}$ (lower) as a function of the resonance mass $m_X$, from the combined analysis of the 8 and 13 TeV data. The results obtained at the two centre of mass energies are also shown. Curves corresponding to the scalar and RS graviton hypotheses are shown in left and right columns respectively.

2016, 13 TeV data recorded in 2015, and 8 TeV data. The test statistic is defined as two times the negative logarithm of the ratio of the maximum likelihood of a model where independent signal strengths are allowed to that of a model where only one signal strength is used. The test statistic is assumed to have a distribution like that of a $\chi^2$ with $n-1$ degrees of freedom, where $n$ is the number of signal strength parameters in the model. Two g.o.f. tests are performed: in the first only 13 TeV data are considered, while in the second 8 TeV data are also included. When comparing 2015 and 2016 13 TeV data, the compatibility is found to be at the 2.7 standard deviations level, while a compatibility at the level of 2.4 standard deviations is found if 8 TeV data are also included. The effect associated with searching for several signal hypothesis on the distribution of the test statistic is not evaluated, but trial factors similar to those estimated for $p_0$ in Ref.[12] can be expected.

## 12 Summary

A search for the resonant production of high mass photon pairs has been presented. The analysis is based on 12.9 $\text{fb}^{-1}$ of pp collisions collected by the CMS experiment in 2016 at $\sqrt{s} = 13$ TeV. Events containing two photon candidates with transverse momenta above 75 GeV are selected. The mass spectrum above 500 GeV is inspected to search for the production of spin-0 and spin-2 resonances.

Limits on the production of scalar resonances and Randall-Sundrum gravitons in the range where 0.5 TeV $< m_X <$ 4.5 TeV and $\Gamma_X/m_X < 5.6 \times 10^{-2}$ are set using the modified frequentist approach. The results obtained with the 2016 dataset are combined statistically with those obtained in Ref. [12] using data corresponding to 19.7 $\text{fb}^{-1}$ and 3.3 $\text{fb}^{-1}$ recorded at $\sqrt{s} = 8$ and $\sqrt{s} = 13$ TeV respectively.

No significant excess is observed above the predictions from the standard model. Using the LO cross sections from PYTHIA 8.2, RS gravitons with masses below 3.85 and 4.45 TeV are excluded for $\tilde{k} = 0.1$ and 0.2 respectively. For $\tilde{k} = 0.01$, graviton masses below 1.95 TeV are excluded, except for the region between 1.75 TeV and 1.85 TeV. These are, to-date, the most stringent limits on RS graviton production.

## References


[1] L. D. Landau, "On the angular momentum of a system of two photons", *Dokl. Akad. Nauk SSSR* **60** (1948) 207, doi:10.1016/B978-0-08-010586-4.50070-5.

[2] C. N. Yang, "Selection Rules for the Dematerialization of a Particle into Two Photons", *Phys. Rev.* **77** (1950) 242, doi:10.1103/PhysRev.77.242.

[3] G. C. Branco et al., "Theory and phenomenology of two-Higgs-doublet models", *Phys. Rept.* **516** (2012) 1, doi:10.1016/j.physrep.2012.02.002, arXiv:1106.0034.

[4] T. D. Lee, "A Theory of Spontaneous T Violation", *Phys. Rev. D* **8** (1973) 1226, doi:10.1103/PhysRevD.8.1226.

[5] L. Randall and R. Sundrum, "A large mass hierarchy from a small extra dimension", *Phys. Rev. Lett.* **83** (1999) 3370, doi:10.1103/PhysRevLett.83.3370, arXiv:hep-ph/9905221.

[6] H. Davoudiasl, J. L. Hewett, and T. G. Rizzo, "Phenomenology of the Randall-Sundrum Gauge Hierarchy Model", *Phys. Rev. Lett.* **84** (2000) 2080, doi:10.1103/PhysRevLett.84.2080, arXiv:hep-ph/9909255.

[7] N. Craig, J. Galloway, and S. Thomas, "Searching for signs of the second Higgs doublet", (2013). arXiv:1305.2424.

[8] ATLAS Collaboration, "Observation of a new particle in the search for the Standard Model Higgs boson with the ATLAS detector at the LHC", *Phys. Lett. B* **716** (2012) 1, doi:10.1016/j.physletb.2012.08.020, arXiv:1207.7214.

[9] CMS Collaboration, "Observation of a new boson at a mass of 125 GeV with the CMS experiment at the LHC", *Phys. Lett. B* **716** (2012) 30, doi:10.1016/j.physletb.2012.08.021, arXiv:1207.7235.

[10] P. S. B. Dev and A. Pilaftsis, "Maximally symmetric two Higgs doublet model with natural standard model alignment", (2014). arXiv:1408.3405.

[11] ATLAS Collaboration, "Search for resonances in diphoton events at $\sqrt{s} = 13$ TeV with the ATLAS detector", (2016). arXiv:1606.03833. Submitted to *J. High Energy Phys.*

[12] CMS Collaboration, "Search for resonant production of high-mass photon pairs in proton-proton collisions at $\sqrt{s} = 8$ and 13 TeV", *Phys. Rev. Lett.* **117** (2016) 051802, doi:10.1103/PhysRevLett.117.051802, arXiv:1606.04093.

[13] ATLAS Collaboration, "Search for high-mass diphoton resonances in pp collisions at $\sqrt{s} = 8$ TeV with the ATLAS detector", *Phys. Rev. D* **92** (2015) 032004, doi:10.1103/PhysRevD.92.032004, arXiv:1504.05511.

[14] ATLAS Collaboration, "Search for extra dimensions in diphoton events using proton-proton collisions recorded at $\sqrt{s} = 7$ TeV with the ATLAS detector at the LHC", *New J. Phys.* **15** (2013) 043007, doi:10.1088/1367-2630/15/4/043007, arXiv:1210.8389.

[15] ATLAS Collaboration, "Search for high-mass dilepton resonances in pp collisions at $\sqrt{s} = 8$ TeV with the ATLAS detector", *Phys. Rev. D* **90** (2014) 052005, doi:10.1103/PhysRevD.90.052005, arXiv:1405.4123.

[16] ATLAS Collaboration, "Search for dilepton resonances in pp collisions at $\sqrt{s} = 7$ TeV with the ATLAS detector", *Phys. Rev. Lett.* **107** (2011) 272002, doi:10.1103/PhysRevLett.107.272002, arXiv:1108.1582.

[17] ATLAS Collaboration, "Search for new phenomena in the $WW$ to $\ell\nu\ell'\nu'$ final state in pp collisions at $\sqrt{s} = 7$ TeV with the ATLAS detector", *Phys. Lett. B* **718** (2013) 860, doi:10.1016/j.physletb.2012.11.040, arXiv:1208.2880.

[18] ATLAS Collaboration, "Search for resonant diboson production in the $WW/WZ \to \ell\nu jj$ decay channels with the ATLAS detector at $\sqrt{s} = 7$ TeV", *Phys. Rev. D* **87** (2013) 112006, doi:10.1103/PhysRevD.87.112006, arXiv:1305.0125.

[19] CMS Collaboration, "Search for diphoton resonances in the mass range from 150 to 850 GeV in pp collisions at $\sqrt{s} = 8$ TeV", *Phys. Lett. B* **750** (2015) 494, doi:10.1016/j.physletb.2015.09.062, arXiv:1506.02301.

[20] CMS Collaboration, "Search for signatures of extra dimensions in the diphoton mass spectrum at the Large Hadron Collider", *Phys. Rev. Lett.* **108** (2012) 111801, doi:10.1103/PhysRevLett.108.111801, arXiv:1112.0688.

[21] CMS Collaboration, "Search for physics beyond the standard model in dilepton mass spectra in proton-proton collisions at $\sqrt{s} = 8$ TeV ", *JHEP* **04** (2015) 025, doi:10.1007/JHEP04(2015)025, arXiv:1412.6302.

[22] CMS Collaboration, "Search for heavy narrow dilepton resonances in pp collisions at $\sqrt{s} = 7$ TeV and $\sqrt{s} = 8$ TeV", *Phys. Lett. B* **720** (2013) 63, doi:10.1016/j.physletb.2013.02.003, arXiv:1212.6175.

[23] CMS Collaboration, "Search for narrow resonances decaying to dijets in proton-proton collisions at $\sqrt{s} = 13$ TeV", *Phys. Rev. Lett.* **116** (2016) 071801, doi:10.1103/PhysRevLett.116.071801, arXiv:1512.01224.

[24] CMS Collaboration, "Search for narrow resonances using the dijet mass spectrum in pp collisions at $\sqrt{s} = 8$ TeV", *Phys. Rev. D* **87** (2013) 114015, doi:10.1103/PhysRevD.87.114015, arXiv:1302.4794.

[25] CMS Collaboration, "Search for narrow resonances in dijet final states at $\sqrt{s} = 8$ TeV with the novel CMS technique of data scouting", (2016). arXiv:1604.08907. Submitted to *Phys. Rev. Lett.*

[26] CMS Collaboration, "Search for resonances and quantum black holes using dijet mass spectra in proton-proton collisions at $\sqrt{s} = 8$ TeV", *Phys. Rev. D* **91** (2015) 052009, doi:10.1103/PhysRevD.91.052009, arXiv:1501.04198.

[27] CMS Collaboration, "Search for massive resonances in dijet systems containing jets tagged as W or Z boson decays in pp collisions at $\sqrt{s} = 8$ TeV", *JHEP* **08** (2014) 173, doi:10.1007/JHEP08(2014)173, arXiv:1405.1994.

[28] CMS Collaboration, "Search for exotic resonances decaying into WZ/ZZ in pp collisions at $\sqrt{s} = 7$ TeV", *JHEP* **02** (2013) 036, doi:10.1007/JHEP02(2013)036, arXiv:1211.5779.

[29] CMS Collaboration, "Search for a narrow spin-2 resonance decaying to a pair of Z vector bosons in the semileptonic final state", *Phys. Lett. B* **718** (2013) 1208, doi:10.1016/j.physletb.2012.11.063, arXiv:1209.3807.

[30] ATLAS Collaboration, "Search for Scalar Diphoton Resonances in the Mass Range 65–600 GeV with the ATLAS Detector in pp Collision Data at $\sqrt{s} = 8$ TeV", *Phys. Rev. Lett.* **113** (2014) 171801, doi:10.1103/PhysRevLett.113.171801, arXiv:1407.6583.

[31] CMS Collaboration, "Performance of photon reconstruction and identification with the CMS detector in proton-proton collisions at $\sqrt{s} = 8$ TeV", *JINST* **10** (2015) P08010, doi:10.1088/1748-0221/10/08/P08010, arXiv:1502.02702.

[32] CMS Collaboration, "Particle-flow event reconstruction in CMS and performance for jets, taus, and $E_{\mathrm{T}}^{\mathrm{miss}}$", CMS Physics Analysis Summary CMS-PAS-PFT-09-001, 2009.

[33] CMS Collaboration, "Commissioning of the particle-flow event with the first LHC collisions recorded in the CMS detector", CMS Physics Analysis Summary CMS-PAS-PFT-10-001, 2010.

[34] CMS Collaboration, "The CMS experiment at the CERN LHC", *JINST* **3** (2008) S08004, doi:10.1088/1748-0221/3/08/S08004.

[35] T. Sjöstrand et al., "An Introduction to PYTHIA 8.2", *Comput. Phys. Commun.* **191** (2015) 159, doi:10.1016/j.cpc.2015.01.024, arXiv:1410.3012.

[36] NNPDF Collaboration, "Parton distributions with LHC data", *Nucl. Phys. B* **867** (2013) 244, doi:10.1016/j.nuclphysb.2012.10.003, arXiv:1207.1303.

[37] T. Gleisberg et al., "Event generation with SHERPA 1.1", *JHEP* **02** (2009) 007, doi:10.1088/1126-6708/2009/02/007, arXiv:0811.4622.

[38] J. Alwall et al., "The automated computation of tree-level and next-to-leading order differential cross sections, and their matching to parton shower simulations", *JHEP* **07** (2014) 079, doi:10.1007/JHEP07(2014)079, arXiv:1405.0301.

[39] GEANT4 Collaboration, "GEANT4 — a simulation toolkit", *Nucl. Instrum. Meth. A* **506** (2003) 250, doi:10.1016/S0168-9002(03)01368-8.

[40] CMS Collaboration, "Observation of the diphoton decay of the Higgs boson and measurement of its properties", *Eur. Phys. J. C* **74** (2014) 3076, doi:10.1140/epjc/s10052-014-3076-z, arXiv:1407.0558.

[41] T. Junk, "Confidence level computation for combining searches with small statistics", *Nucl. Instr. and Meth. A* **434** (1999) 435, doi:10.1016/S0168-9002(99)00498-2, arXiv:hep-ex/9902006.

[42] A. L. Read, "Presentation of search results: the $CL_s$ technique", *J. Phys. G* **28** (2002) 2693, doi:10.1088/0954-3899/28/10/313.

[43] LHC Higgs Combination Group, "Procedure for the LHC Higgs boson search combination in Summer 2011", Technical Report CMS-NOTE-2011-005, ATL-PHYS-PUB-2011-11, 2011.

[44] G. Cowan, K. Cranmer, E. Gross, and O. Vitells, "Asymptotic formulae for likelihood-based tests of new physics", *Eur. Phys. J. C* **71** (2011) 1554, doi:10.1140/epjc/s10052-011-1554-0, arXiv:1007.1727.